Modeling Interplanetary Expansion and Deformation of CMEs with ANTEATR-PARADE I: Relative Contribution of Different Forces

C. Kay[1,2], T. Nieves-Chinchilla[1]

[1]Heliophysics Science Division, NASA Goddard Space Flight Center, Greenbelt, MD, USA
[2]Dept. of Physics, The Catholic University of America, Washington DC, USA

Key Points:

- ANTEATR-PARADE adds CME expansion and deformation to the interplanetary drag model
- Internal CME magnetic forces tend to have less of an effect than external drag forces
- The initial expansion velocity has a very strong effect on the total amount of deformation

Corresponding author: Christina Kay, ckay@gmail.com

Abstract

Coronal Mass Ejections (CMEs) are key drivers of space weather activity but most predictions have been limited to the expected arrival time of a CME, rather than the internal properties that affect the severity of an impact. Many properties, such as the magnetic field density and mass density, follow conservation laws and vary systematically with changes in the size of a CME. We present ANTEATR-PARADE, the newest version of the ANTEATR arrival time model, which now includes physics-driven changes in the size and shape of both the CME's central axis and its cross section. Internal magnetic and external drag forces affect the acceleration of the CME in different directions, inducing asymmetries between the radial and perpendicular directions. These improvements should lead to more realistic CME velocities, both bulk and expansion, sizes and shapes, and internal properties. ANTEATR-PARADE is the first model of its kind that provides this level of detail on the time scales needed for future space weather predictions. We present the model details, an initial illustration of the general behavior, and a study of the relative importance of the different forces. The model shows a pancaking of both the cross section and central axis of the CME so that their radial extent becomes smaller than their extent in the perpendicular direction. For a single parameterization of our magnetic field model we find that the drag forces tend to exceed the magnetic forces and the results are very sensitive to the initial velocities of the CME.

Plain Language Summary

Coronal Mass Ejections (CMEs) are large explosions of matter and magnetic field that violently erupt from the Sun. When they hit the Earth they can cause negative effects in human technology so it is important to be able to forecast them. Most models of CMEs only predict if and when a CME could impact the Earth but not the properties of a CME that may affect how severe the impact will be. Many of these properties scale with the CME size and shape so we need to understand how the CME expands between the Sun and the Earth. We have taken a model for the arrival time and added new forces that allow us to better understand the evolution of a CME's size and shape. This should help us better predict factors like magnetic field strength, number density, and velocity. Our model reproduces a previously known trend of CMEs becoming squished in the radial direction or "pancaking." We explore which forces are the most important for causing this effect. For the current model set up, we find that drag forces are more important than magnetic forces, but this may change with a different magnetic field model. We also see that the model results depend strongly on how we initially convert the total CME speed into initial propagation and expansion speeds.

1 Introduction

Understanding the interplanetary behavior of CMEs is critical for accurate space weather forecasting. The severity of a geomagnetic storm depends on the CME properties at the time of impact, mostly significantly the magnetic field but also its size and kinematic properties. Accordingly, we must not only understand the properties with which a CME is initiated, but how they evolve during its propagation if we wish to know the severity and timing of an impact. Kilpua et al. (2019) provides an in depth summary on many of the challenges of forecasting CMEs.

We tend to have an abundance of coronal images from the Earth's perspective, both in visible light and the extreme ultraviolet, which have allowed us to study the source region and early evolution of Earth-impacting CMEs for nearly half of a century (e.g., Tousey, 1973), but routine observations from off the Sun-Earth line are limited to the coronagraphs or heliospheric imagers on the STEREO satellites. Parker Solar Probe and Solar Orbiter will provide exciting remote observations from new angles and distances

but will not give the consistent off-axis perspective needed to better understand the interplanetary evolution of CMEs.

In contrast, situ observations yield a single path through a CME, but it is often unclear where a satellite intersects a CME, or even which CME it is during times of high activity. Tying these observations together requires accurate modelling of a CME from the corona and through interplanetary space. Many case studies exist where large teams are able to work together to piece together the full Sun-to-Earth behavior of a single CME (e.g., Möstl et al., 2015; Patsourakos et al., 2016; Palmerio et al., 2018; Heinemann et al., 2019) but currently this is only done long after a CME's passage.

The vast majority of interplanetary CME models focus solely on predicting their arrival time at Earth (e.g., Vršnak et al., 2013; Möstl et al., 2015; Paouris & Mavromichalaki, 2017; Liu et al., 2018), which is an essential goal for space weather forecasting. Arrival time models can be highly successful for forecasting but not lead to an improved understanding of the actual physics if they are empirical models fine-tuned to yield accurate results or highly-layered, machine-learning models that are opaque to their users.

The physics-driven drag models tend to treat the CME as a simplified structure and incorporate the effects of the standard drag equation in either one or two dimensions (e.g., Vršnak et al., 2013; Hess & Zhang, 2015; Möstl et al., 2015; Rollett et al., 2016; Napoletano et al., 2018). This is clearly an oversimplification of the actual physical processes at play. For example, M. J. Owens et al. (2017) argue that CMEs cannot be a coherent structure on large scales since their expansion speeds often exceed the local Alfven speed so information cannot be propagating over the full structure. These sort of toy models, however, run on the time scales needed for space weather prediction and have shown to be useful in predicting arrival times (e.g., Riley et al., 2018; Wold et al., 2018) while providing some level of physical intuition about the evolutionary processes.

Most of the models designed with predictions in mind focus solely on the arrival time of the CME, and possibly velocity, but do not provide a complete picture of the internal CME properties. Recently, Mishra and Wang (2018) developed a model that simulates the internal thermodynamics of a CME during coronal propagation. This model uses the observed CME speeds in combination with Lorentz, thermal, and centrifugal forces to determine the relative importance of each as well as the thermodynamic properties. Mishra and Wang (2018) only present coronal results for a single observed CME but develop a method that could be useful for forward modelling many of the internal CME properties out to greater distances.

Interplanetary studies show that CMEs commonly become oblate during propagation so that their extent in the radial direction is much shorter than their extent in the direction perpendicular to the radial (hereafter perpendicular direction). This effect is often referred to as "pancaking." Pancaking can be directly seen in simulations of various complexity (Riley & Crooker, 2004; Riley et al., 2004; Savani et al., 2011) and an oblate cross section can also be inferred from in situ observations of properties such as the shock standoff distance (Russell & Mulligan, 2002) or the direction flow in the sheath between the CME and shock (M. Owens & Cargill, 2004).

Previous studies have simulated the pancaking of a CME's cross section by assuming that all parts of it are convected out at the same speed in the local radial direction (Riley & Crooker, 2004; M. J. Owens et al., 2005). This naturally causes the CME to maintain a constant angular width, however, the distance between two points along the same radial direction will remain constant as they move at the same speed. This causes the aspect ratio to change since the cross section grows in the perpendicular direction while remaining fixed in the radial direction.

Some models of the magnetic field of a CME can incorporate this ellipticity of the cross section (Mulligan & Russell, 2001; Hidalgo et al., 2002; Isavnin, 2016; Nieves-Chinchilla

et al., 2018). The majority of the elliptical magnetic field models are designed to be fit to observations by adjusting their free parameters in response to some sort of error minimization technique, rather than being used to forward model the evolution of a CME's magnetic field. Isavnin (2016) illustrate the extent that evolutionary effects such as pancaking, expansion, and a skew of the central axis can have on the in situ profiles of a CME. Nieves-Chinchilla et al. (2018) introduce the elliptic-cylindrical analytical flux rope model, which is highly flexible in terms of describing a distorted flux rope cross section but simple enough to be of use for derivations that require the full expression of the magnetic field.

Similar to the distortion of the cross section shape, one may expect that the central axis of a CME also distorts during its interplanetary propagation. Janvier et al. (2013) use in situ measurements to infer the local axis orientation of CME from 15 years of WIND observations at 1 AU and compare this with the expected distributions based on the global axis shape. They find that their results are compatible with the expected results for a CME that is 20% wider in the perpendicular direction than it is in the radial direction, but not with a circular shape or greater than a 30% asymmetry. A circular axis is often assumed for any models that are fit to coronal observations (e.g. the Graduated Cylindrical Shell model, Thernisien et al., 2006), suggesting that a pancaking-like effect must occur in this direction in order to tie together the near-Sun and near-Earth measurements. An actual, detailed study of the coronal shapes of CMEs is required to truly understand what the average shape at 1 AU implies for the interplanetary evolution of the central axis.

We have developed a suite of strategically-simplified physics-driven models of CME behavior from the Sun to the Earth, with the intended eventual use for space weather predictions. The Open Solar Physics Rapid Ensemble Information (OSPREI) suite began with Forecasting a CME's Altered Trajectory (ForeCAT, Kay et al., 2015), which modeled the deflection and rotation of a CME in the corona from background magnetic forces. We later developed the ForeCAT In situ Data Observer (FIDO, Kay et al., 2017) to combine a simple flux rope model with ForeCAT results to produce synthetic in situ profiles. These were then linked with ANother Type of Ensemble Arrival Time Results (ANTEATR, Kay & Gopalswamy, 2018; Kay, Mays, & Verbeke, 2020), which determines transit times and velocities using a one-dimensional drag model but full three-dimensional CME shape when determining the precise timing of the impact. In this work, we combine ANTEATR with the magnetic field model of Nieves-Chinchilla et al. (2018) as ANTEATR-PARADE (Physics-driven Approach to Realistic Axis Deformation and Expansion) to develop the first forward model of a CME's interplanetary expansion and deformation that runs efficiently enough to be used for future real-time ensemble predictions. We present a basic description of the model in Section 2 and full details of the force derivations in the Supplementary Material. We then show the general model behavior for CMEs of different strengths and identify which forces are most responsible for the evolution of the CME parameters. A companion paper, Kay and Nieves-Chinchilla (2021) (hereafter Paper II), will perform a full sensitivity study of the model using parameter space explorations to determine the dependence of each output on each input.

2 ANTEATR-PARADE Model

The ANTEATR-PARADE models builds upon the original ANTEATR model by incorporating the internal magnetic forces of the CME and allowing for changes in the axis and cross section (CS) shape. Here we explain the basic components of the model and then describe the general algorithm. More details on nonorthogonal coordinate systems and magnetic forces in those coordinates can be found in the Supplementary Material.

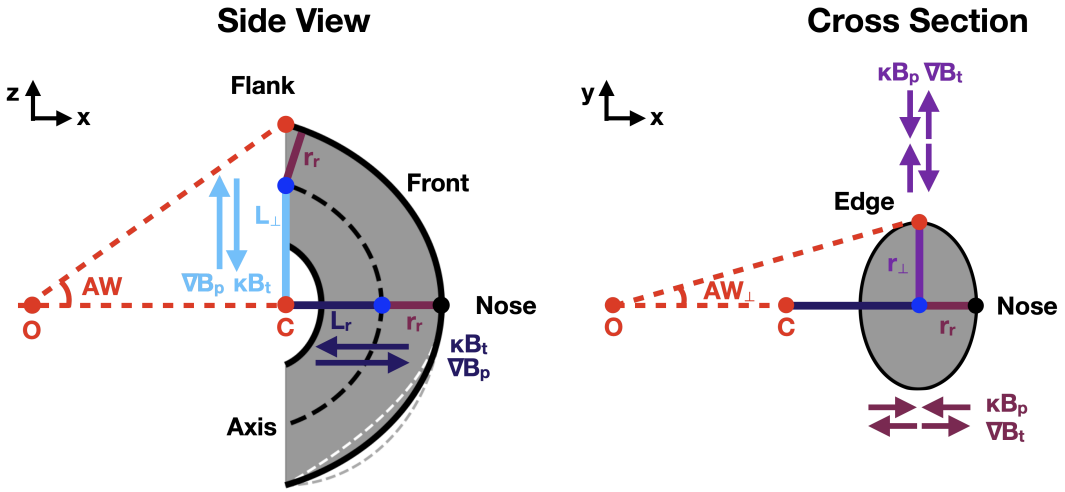

Figure 1. Cartoon showing a side view and the cross section of the torus shape used in ANTEATR-PARADE.

2.1 CME Shape

Previously, the OSPREI suite of models, including ANTEATR, has represented the flux rope of a CME as a torus with an elliptical axis and circular cross section. Figure 1 shows a side view of our new CME shape (left) and a view of the CS (right). In this cartoon, the $\hat{x}$ direction represents the radial direction at the CME nose, $\hat{y}$ represents the direction perpendicular to the radial vector in the plane of the CS at the nose, and $\hat{z}$ represents the direction perpendicular to the $\hat{x}$ in the plane containing the CME axis.

The first major change is to allow the CS to be an ellipse instead of restricting it to a circle, as shown on the right side of Fig. 1. The CS is now defined by the radius in the radial direction, r_r, and the perpendicular radius, $r_\perp$. We define the ratio of the radii as $\delta_{CS} = r_r/r_\perp$. The perimeter of the cross section is given by

$$\begin{aligned} x &= \delta_{CS} r_\perp \cos\psi \\ y &= \quad r_\perp \sin\psi \end{aligned} \tag{1}$$

where ψ is used for parameterization. The regions within the cross section are described by Equation 1 with $r_\perp$ replaced by the coordinate r, which varies between 0 and $r_\perp$. We emphasize that, unless $\delta_{CS} = 1$, r and ψ are not equivalent to a polar coordinate system with the origin at the center of the cross section. They form a nonorthogonal coordinate system and must be treated appropriately using covariant and contravariant coordinates and a tensorial analysis when calculating forces. The gist of the ANTEATR-PARADE model and certainly its results can be understood without these details so we only include them in the supplementary material and present a simplified description here. We caution the reader, however, on their own application of the equations in Section 2 without consulting the supplementary material.

The second major change is in the shape of the toroidal axis. The toroidal axis is represented by the dashed black line in Fig. 1 and the blue dots lie along it in the direction of the nose and the flank. We previously represented the axis as half of an ellipse defined by the lengths in the radial and perpendicular directions, now called L_r and $L_\perp$, which extend from the center of the CME (marked with a red dot and a 'C') to the blue

dots on the toroidal axis. Analogous to the CS, we define $\delta_{Ax} = L_r/L_\perp$. An elliptical axis is then given by

$$\begin{aligned} x &= \delta_{Ax} L_\perp \cos\phi \\ z &= \quad L_\perp \sin\phi \end{aligned} \tag{2}$$

where ϕ is another ellipse parameterization and not a polar angle.

Typically, L_r is the semi-minor axis and the toroidal axis is squashed in the radial direction relative to the perpendicular direction. For a full ellipse, the curvature at semi-major axis is greater than the curvature at the semi-minor axis. This corresponds to higher curvature at the CME flank than the CME nose. The precise behavior of a CME shape near the flanks is not yet fully understood but coronagraph images do not suggest it should be as tightly curved as a full ellipse.

Alternatively, we can approximate the axis as the parabola that intersects the same two blue dots as the previous ellipse. This parabola is given by

$$x = \delta_{Ax} L_\perp - \frac{\delta_{Ax}}{L_\perp} z^2 \tag{3}$$

This significantly increases the curvature at the nose while significantly decreasing it near the flank, likely beyond what is reasonable at either location. We form a hybrid shape, taking the average of the ellipse and the parabola to yield

$$\begin{aligned} x &= \delta_{Ax} L_\perp \cos\phi \\ z &= \frac{1}{2} L_\perp \left(\sin\phi + \sqrt{1 - \cos\phi} \right) \end{aligned} \tag{4}$$

which we derive by parameterizing Eq. 3 with θ such that $z = L_\perp \sin\theta$ and relating ϕ and θ by finding where the two shapes give the same x value. This causes a more gentle variation in the curvature with slightly stronger curvature at the nose than the edges.

The axial magnetic tension force we calculate (details in Section 2.3) is quite sensitive to the curvature but these shapes are really quite similar visually. Fig. 1 shows the actual hybrid axis shape. The dashed white and grey lines interior and exterior to the CME front on the bottom of the side view in Fig. 1 show the change in the front for the parabola and ellipse axis, respectively. This is a very minor change in the apparent shape that cannot be constrained by current observations. Our use of the hybrid shape is fully motivated by it yielding the most stable forces during model development.

The toroidal axis defines the orientation of the CS as we define the CS to be perpendicular to the axis. At the nose this is the xy-plane, as shown in the Fig. 1, but it rotates toward the yz-plane as one moves along the axis. The normal direction to the axis can be calculated from the parametric definition of the axis. A general solution exists, but is quite convoluted. At the flank, the CS plane is not the yz-plane (note the orientation of the maroon line showing r_r at the flank in Fig. 1). Instead, we find that it is at an angle $\theta_n = \tan^{-1}(4\delta_{Ax})$ with respect to the x-axis. For δ_{Ax} between 0.7 and 0.9 this corresponds to θ_n between 70.3° and 74.5°.

Fully determining the CME shape requires the four lengths r_r, $r_\perp$, L_r, and $L_\perp$. Alternatively, we can define it using two angular widths, AW and $AW_\perp$, the shape values δ_{CS} and δ_{Ax}, and the radial distance of the front of the CME, R_F, which may be more tangible or at least easier to determine from standard techniques for fitting CMEs in coronagraph images. AW is the width in the side view, sometimes referred to as the face-on width, and $AW_\perp$ is the width of the CS, sometimes referred to as the edge-on width. Both are measured with respect to an origin at the center of the Sun (red 'O' in Fig. 1).

2.2 Magnetic Field

ANTEATR-PARADE uses the elliptic-cylindrical flux rope model from Nieves-Chinchilla et al. (2018) (hereafter, NC18) for the CME's magnetic field. NC18 solve the Maxwell equations for a generalized expression of the magnetic field in the nonorthongonal elliptical coordinate system. NC18 assume that there is no radial component of the magnetic field in the direction normal to the ellipse and that there are no changes in values along the cylindrical axis (analogous to our toroidal axis). By expressing the components of the current density as polynomials that depend only on r, NC18 derive an expression for the magnetic field components

$$\begin{aligned} B_r &= 0 \\ B_t &= \sum_{n=1}^{\infty} \delta_{CS} B_n^0 [\tau - \bar{r}^{n+1}] \\ B_p &= -\sum_{m=0}^{\infty} \frac{(n+1)\delta_{CS}\sqrt{\delta_{CS}^2 \sin^2\psi + cos^2\psi}}{\delta_{CS}^2 + m + 1} \frac{B_n^0}{C_{nm}} \bar{r}^{m+1} \end{aligned} \tag{5}$$

where the NC18 B^y and B^ψ components correspond directly to our toroidal field, B_t, and poloidal field, B_p. In Equation 5, n and m are the order of the polynomial components, B_n^0 determines the magnetic field strength, τ determines the ratio of the the toroidal field at the center of the CS versus the edge, and C_{nm} determines the ratio of the toroidal and poloidal magnetic field. $\bar{r}$ is the fractional radial distance that varies between 0 at the center and 1 at the edge.

As in NC18, we restrict our magnetic field to [m,n] = [0,1] so that the expressions for the magnetic field becomes

$$\begin{aligned} B_r &= 0 \\ B_t &= \delta_{CS} B_0 [\tau - \bar{r}^2] \\ B_p &= -\frac{2\delta_{CS}\sqrt{\delta_{CS}^2 \sin^2\psi + cos^2\psi}}{1 + \delta_{CS}^2} \frac{B_0}{C} \bar{r} \end{aligned} \tag{6}$$

, where we have replaced B_1^0 and C_{10} with B_0 and C for readability since we are only considering single values for m and n. Future work will explore the effects of different values of [m,n] on the ANTEATR-PARADE model.

2.3 Magnetic Forces

ANTEATR-PARADE calculates magnetic forces which act to both expand and deform the CME axis and CS. We calculate the magnetic tension and magnetic pressure gradients from both B_t and B_p. The colored arrows in Fig. 1 show the direction of these forces relative to the CME shapes. For the CS, the poloidal magnetic tension (labeled κB_p) will cause inward constriction whereas the toroidal magnetic gradient will cause outward expansion (labeled ∇B_t) and are functions of ψ, in general, and can vary between the nose (maroon arrows) and the edge (purple arrows). The toroidal magnetic tension (labeled κB_t) from the curved toroidal axis will cause it to move inward whereas the poloidal pressure gradient or hoop force (labeled ∇B_p) will cause outward motion. As with the CS, we may not have a balance between the axis force at the nose (blue arrows) and the flank (light blue arrows). For both the CS and toroidal axis, an imbalance in magnetic tension and pressure will cause expansion (changing AW and $AW_\perp$ and if the expansion is not balanced in different directions then δ_{CS} and δ_{Ax} will also change.

Determining these forces requires careful analysis in the nonorthogonal coordinate system. Here we present an overview of the process, full details are in the supplementary material. We start with the expression for the Lorentz force in terms of the current

density and magnetic field from NC18 (Eq. 27). This equation is for a cylinder, rather than a curved tube, and the force points entirely in the r direction, which is the normal to the ellipse at that particular ψ. We consider the forces from the axial curvature separately. We then use Ampere's law (Eqs. 13 and 14 in NC18) to replace the current density in the Lorentz force with derivatives of the magnetic field. This expression can be rearranged to contain terms analogous to the magnetic tension and magnetic pressure gradient forces one finds in an orthogonal coordinate system. These forces act on the CS with the poloidal tension constricting it and the toroidal gradient causing expansion, assuming that it exceeds the inward pressure gradient of the solar wind that we also include. For our chosen values of [m,n] = [0,1] the poloidal pressure gradient terms go to zero.

We consider a thin segment of the toroidal axis of width $R_\kappa d\phi$, where R_κ is the local radius of curvature of the axis, and a wedge of width $r d\psi$ within this segment. The total force on this wedge is the Lorentz force per volume integrated over r, which we set equal to an acceleration multiplied by the density and the volume of the wedge. This gives us the acceleration of the edge of CS, a_{CS}.

$$a_{CS} = \frac{\delta_{CS}^2 B_0^2}{\pi \rho r_\perp} \left[\frac{2}{3(1+\delta_{CS}^2)C^2} - \left(\frac{1}{3}\tau - \frac{1}{5} \right) \right] - \frac{B_{SW}^2}{8\pi r_\perp} \tag{7}$$

This expression includes the inward pressure from the external solar wind magnetic field, unlike the version in the supplementary material which only includes the internal magnetic forces. This is the change in the normalized parametric r and it does not depend on ψ, meaning that while these forces can cause the CS to grow to contract, the actual shape, defined by δ_{CS}, will not change. This is specific to our chosen [m,n] = [0,1] and not necessarily true for any other combination.

Curving the cylindrical axis introduces an inward tension force from toroidal magnetic field and an outward hoop force from the poloidal field. To conserve magnetic flux, the poloidal field is enhanced on the side of the CS toward the center of curvature due to the decrease in area from the axial curvature. The opposite occurs on the side of the CS near the front of the CME, creating a outward gradient force. Welsch (2018) present a derivation of the hoop force in relation to the low coronal dynamics of CMEs for a CME with circular CS and circular axis. Welsch (2018) consider a segment of the torus with width $R d\phi$, where R is the radius of their circle (and the radius of curvature). We take a similar approach but consider a segment $R_c d\phi$ where R_c is the local radius of curvature for the toroidal axis at some ϕ. The magnitude of the toroidal field is unchanged but the poloidal field scales as

$$B_p' = B_p \frac{R_c}{R_c + \delta_{CS} r_\perp \bar{r} \cos\psi} \tag{8}$$

where B_p' is the poloidal field for a curved toroidal axis.

We approximate the segment as locally elliptic-cylindrical and use the poloidal pressure gradient terms of the Lorentz force in elliptic-cylindrical coordinates, which no longer go to zero. This leads to an acceleration of the toroidal axis of

$$a_{hoop} = \frac{B_0^2}{\pi \rho C^2 R_c} \frac{\sqrt{1-\delta_{CS}^2\gamma^2}(\delta_{CS}^2\gamma^2 - 6) + 6 - 4\delta_{CS}^2\gamma^2}{\delta_{CS}^3\gamma^2(1+\delta_{CS}^2)^2\sqrt{1-\delta_{CS}^2\gamma^2}} \tag{9}$$

where $\gamma = r_\perp / R_C(\phi)$ has been used to simply the expression.

For the axial magnetic tension we again consider a segment $R_c d\phi$ and use a curvature of $\kappa = 1/R_c$. The acceleration from the axial tension force is

$$a_{\kappa Bt} = \frac{\delta_{CS} B_0^2}{4\pi \rho R_c} \left(\tau^2 - \tau + \frac{1}{3} \right) \tag{10}$$

which has a dependence on ϕ through the radius of curvature. Both the axial tension and hoop forces have a dependence on ϕ so the axial magnetic forces can change the shape and δ_{Ax} as well as causing expansion or contraction. Note that both these accelerations point in the direction normal to the toroidal axis. At the nose the normal direction is parallel to $\hat{x}$ so the forces fully contribute to expanding or contracting L_r. At the flank the normal is not parallel to $\hat{z}$ so $\sin(\theta_n)$ of the acceleration for ϕ =90° affects $L_\perp$ but $\cos(\theta_n)$ of it affects L_r.

The magnetic forces give the expansion or contraction of the toroidal axis and CS, encompassing the internal magnetic forces. While the above equations hold over all ϕ and ψ we only use the values at the nose and edge for the axis and similarly only along the two axes of the CS. From the magnetic forces, we determine the change in the four length parameters defining the CME shape.

$$\begin{aligned}
\frac{\partial^2 r_r}{\partial t^2} &= \delta_{CS} a_{CS} \\
\frac{\partial^2 r_\perp}{\partial t^2} &= a_{CS} \\
\frac{\partial^2 L_r}{\partial t^2} &= a_{hoop,n} + a_{\kappa Bt,n} - (a_{hoop,f} + a_{\kappa Bt,f}) \cos\theta_n \\
\frac{\partial^2 L_\perp}{\partial t^2} &= (a_{hoop,f} + a_{\kappa Bt,f}) \sin\theta_n
\end{aligned} \tag{11}$$

where the last part of the subscript indicates axial accelerations at either the nose or the flank. We subtract the component of the flank acceleration in the x direction as it corresponds to a change in the position of the sunward side of L_r.

2.4 Drag Forces

ANTEATR-PARADE also includes the external drag on the CME. We use the standard hydrodynamic drag equation as was previously done in the original ANTEATR. The force from drag is

$$F_{drag} = -C_d A \rho_{SW} (v - v_{SW}) |v - v_{SW}| \tag{12}$$

where C_d is the dimensionless drag coefficient, A is the cross-sectional area in plane perpendicular to the direction of motion, v is a CME velocity, and v_{SW} is the solar wind velocity, which we assume flows entirely in the radial direction. We determine the drag in three different directions. The first is the radial direction (the x-direction in Fig. 1)

$$F_{d,r} = -C_d A_{FO} \rho_{SW} (v_F - v_{SW}) |v_F - v_{SW}| \tag{13}$$

where v_F is the velocity of the front, which is a combination of the bulk velocity, v_B, the axial expansion in the radial direction $v_{Ax,r}$, and the CS expansion in the radial direction, $v_{CS,r}$.

$$v_F = v_B + v_{Ax,r} + v_{CS,r} \tag{14}$$

The area perpendicular to the radial direction, A_{FO}, is the same as the face-on area, and can be determined from AW and $AW_\perp$.

The second drag force is in direction of the flanks (the z-direction in Fig. 1), affecting the expansion of AW.

$$F_{d,\perp} = -C_d A_\perp \rho_{SW} (v_{F\perp} - \sin AW v_{SW}) |v_{F\perp} - \sin AW v_{SW}| \tag{15}$$

Here, $v_{F\perp}$ is the velocity of the flank, which results from the perpendicular axial expansion, $v_{Ax,r}$, and the component of $v_{CS,r}$ in the z-direction.

$$v_{F,\perp} = v_{Ax,\perp} + v_{CS,r} \sin\theta_n \tag{16}$$

The cross-sectional area for this drag, $A_\perp$, can be determined from $AW_\perp$ and the length of the CME in the radial direction. The final drag force acts on the CS expansion in the perpendicular direction (the y-direction in Fig. 1) and the CME velocity is simply the perpendicular CS expansion velocity, $v_{CS,\perp}$.

$$F_{d,CS,\perp} = -C_d A_{EO} \rho_{SW} (v_{F\perp} - \sin AW_\perp v_{SW}) |v_{F\perp} - \sin AW_\perp v_{SW}| \tag{17}$$

Now the cross sectional area A_{EO} is the same as the edge-on width and can be determined from the toroidal axis length and the radial width of the CS.

The first two drag forces are calculated using v_F and $v_{F,\perp}$ and will clearly cause a change in these velocities but it is less obvious how they affect the individual velocities that make up v_F and $v_{F,\perp}$. The net acceleration of the individual components should add up to the total acceleration. We (somewhat arbitrarily) decide to weight the total drag force by the fractional magnitude of the individual components relative to the total velocity

$$F_{d,r} = \frac{v_B}{v_F} F_{d,r} + \frac{v_{Ax,r}}{v_F} F_{d,r} + \frac{v_{CS,r}}{v_F} F_{d,r} = F_{d,B} + F_{d,Ax,r} + F_{d,CS,r} \tag{18}$$

where $F_{d,B}$, $F_{d,Ax,r}$, and $F_{d,CS,r}$ are the accelerations affecting the bulk, radial axial, and radial CS velocities. $v_{CS,r}$ appears in both the expression for $F_{d,r}$ and $F_{d,\perp}$. We assume that the $F_{d,CS,r}$ found at the nose is the same at the flank, which is an oversimplification for a real CME but allows us to retain a uniform CME CS. We subtract $\sin\theta_n F_{d,CS,r}$ from $F_{d,\perp}$ so that the remaining force is the drag on the axis in the perpendicular direction $F_{d,Ax,\perp}$

2.5 Initial Velocity

Typically, we begin a simulation at 10 R_s as this is roughly where the external magnetic forces of the corona tend to become negligible. ANTEATR-PARADE is designed to take output from ForeCAT, our coronal deflection and rotation model, which we typically run out to 10 R_s. The internal forces may very well be important below this height, future work will incorporate them into the ForeCAT model and Paper II will study the sensitivity of ANTEATR-PARADE to small changes in R_F.

This means that our initial parameters should describe the CME at 10 R_s. We only require the initial velocity of the CME front, which is often all that is easily measurable from a coronagraph image, which then needs to separated into $v_{CS,r}$, $v_{CS,\perp}$, $v_{Ax,r}$, $v_{Ax,\perp}$, and v_B. The first approach is to assume that the CME is undergoing convective pancaking and extrapolate the approach of Riley and Crooker (2004) and M. J. Owens et al. (2005) to the full 3D torus structure. If the CME front is moving at v_F and we assume constant angular widths AW and $AW_\perp$ then the lengths defining the CME shape change as

$$\begin{aligned}
r_r &= r_{r,0} + v_{CS,r} t &&= r_{r,0} + v_F (1 - \cos AW_\perp) t \\
r_\perp &= r_{\perp,0} + v_{CS,\perp} t &&= r_{\perp,0} + v_F \sin AW_\perp t \\
L_r &= L_{r,0} + v_{Ax,r} t &&= L_{r,0} + v_F (\cos AW - \cos AW_\perp) t \\
L_\perp &= L_{\perp,0} + v_{Ax,\perp} t &&= L_{\perp,0} + v_F \left(\sin AW - \frac{1 - \cos AW_\perp}{\sin \theta_n} \right) t
\end{aligned} \tag{19}$$

where the subscript 0 indicates initial values. Unlike M. J. Owens et al. (2005) we do not include any internal expansion within the convective velocity model since it is incorporated through our magnetic forces.

Alternatively, we can assume that the CME is initially fully self-similar and that both the angular widths, AW and $AW_\perp$, and aspect ratios, δ_{CS} and δ_{Ax} remain constant in the absence of any forces. The front of the CME is initially at $R_{F0} = R_{C0} +$

L_{r0}+r_{r0}, where R_{C0} is the initial radial distance of the center of the CME (labeled with a C in Fig. 1) and not a radius of curvature. The lengths evolve kinematically, the same as for the convective velocities, but now the initial velocities are

$$\begin{aligned} v_{CS,r} &= v_F \frac{r_{r0}}{R_{F0}} \\ v_{CS,\perp} &= v_F \frac{r_{\perp 0}}{R_{F0}} \\ v_{Ax,r} &= v_F \frac{L_{r0}}{R_{F0}} \\ v_{Ax,\perp} &= v_F \frac{L_{\perp 0}}{R_{F0}} \end{aligned} \tag{20}$$

. For both the convective and self-similar approach, we use the model only to set the initial CME velocities and beyond this all velocities evolve according to the forces acting upon the CME.

These two options likely represent the two extremes of the possible values for a real CME, the "correct" values are probably not either, but somewhere in between. For now we do not have a definitive value from observations, and finding one from image analysis is a major undertaking, if at all possible, and far beyond the scope of this work. Here we consider both options for decomposing the front velocity into component velocities. In Paper II we present a method for varying between fully convective and fully self-similar and analyze the effect of the IVD on the outputs.

2.6 ANTEATR-PARADE Algorithm

We now have all the components necessary to build the basic algorithm of ANTEATR-PARADE. The model requires the initial speed of the CME front, v_F, the CME mass, M_{CME}, AW, $AW_\perp$, δ_{CS}, δ_{Ax}, the CME magnetic field strength relative to the background solar wind, and the properties of background solar wind at 1 AU. We first determine the initial values of r_r, $r_\perp$, L_r, and $L_\perp$. We then determine corresponding expansion velocities, $v_{CS,r}$, $v_{CS,\perp}$, $v_{Ax,r}$, and $v_{Ax,\perp}$ according to the choice of initial velocity model (convective or self-similar).

Then, for each time step Δt, the magnetic and drag forces are determined and parameters updated as follows

$$\begin{aligned} \Delta r_r &= v_{CS,r}\Delta t + \frac{1}{2}(\delta_{CS}a_{CS} + a_{d,CS,r})\Delta t^2 \\ \Delta r_\perp &= v_{CS,\perp}\Delta t + \frac{1}{2}(a_{CS,\perp} + a_{d,CS,\perp})\Delta t^2 \\ \Delta L_r &= v_{Ax,r}\Delta t + \frac{1}{2}\left[(a_{hoop,f} + a_{\kappa Bt,f}) - \cos\theta_n\left(a_{hoop,f} + a_{\kappa Bt,f}\right) + a_{d,Ax,r}\right]\Delta t^2 \\ \Delta L_\perp &= v_{Ax,\perp}\Delta t + \frac{1}{2}\left[\sin\theta_n\left(a_{hoop,f} + a_{\kappa Bt,f}\right) + a_{d,Ax,\perp}\right]\Delta t^2 \\ \Delta R_F &= v_F\Delta t + \frac{1}{2}\left[\delta a_{CS} + (a_{hoop,f} + a_{\kappa Bt,f}) - \cos\theta_n\left(a_{hoop,f} + a_{\kappa Bt,f}\right) + a_{d,r}\right]\Delta t^2 \\ \Delta v_{CS,r} &= (\delta_{CS}a_{CS} + a_{d,CS,r})\Delta t \\ \Delta v_{CS,\perp} &= (a_{CS,\perp} + a_{d,CS,\perp})\Delta t \\ \Delta v_{Ax,r} &= \left[(a_{hoop,f} + a_{\kappa Bt,f}) - \cos\theta_n\left(a_{hoop,f} + a_{\kappa Bt,f}\right) + a_{d,Ax,r}\right]\Delta t \\ \Delta v_{Ax,\perp} &= \left[\sin\theta_n\left(a_{hoop,f} + a_{\kappa Bt,f}\right) + a_{d,Ax,\perp}\right]\Delta t \\ \Delta v_F &= \left[\delta a_{CS} + (a_{hoop,f} + a_{\kappa Bt,f}) - \cos\theta_n\left(a_{hoop,f} + a_{\kappa Bt,f}\right) + a_{d,r}\right]\Delta t \end{aligned} \tag{21}$$

where the drag accelerations, $a_{d,i}$, are determined from the corresponding forces $F_{d,i}$ by dividing by the CME mass. The CME density and magnetic field are then updated by assuming mass and magnetic flux conservation. We have two relations from the fluxes from B_t and B_p but three variables than can evolve to maintain flux conservation and

are not already determined elsewhere in the model. The total magnetic field strength, B_0 is an obvious choice to have evolve but the system is underdetermined to calculate both τ and C. For now, we assume that τ remains constant and C changes, roughly implying that the distribution of the toroidal field within a CME remains constant but the ratio of toroidal to poloidal magnetic field can evolve. We note that Florido-Llinas et al. (2020) find that only certain combinations of C and τ are stable with respect to the kink instability. Our model will not exhibit the same instabilities since we only calculate forces along specific axes but we will identify where these limits occur.

A simulation runs until the CME nose reaches a user-specified final distance. For now, all impacts occur at the CME nose (both ϕ and ψ of 0°). Future work will explore the effect of oblique impacts on the expected CME observables and fully develop the generation of in situ profiles.

For the background solar wind, we currently require the 1 AU values of the solar wind density, velocity, and total magnetic field strength, which we use to scale values at closer distances to the Sun. The solar wind velocity treated as constant and the density scales inversely with the distance squared. For the magnetic field we use a simple Parker spiral model.

3 Ensemble Study Description

This paper presents the first results from the ANTEATR-PARADE model and our focus is on understanding the relative importance of the different forces, both magnetic and drag, as well as understanding the actual CME evolution. We look to compare results using four different magnetic forces configurations - no magnetic forces, only the toroidal pressure gradient that causes CS expansion, both the CS pressure gradient and tension forces, or full CS and axial forces. The case with out the CS tension mirrors much of the early work done on pancaking where only an outward pressure gradient is included. We run each of the four magnetic force configurations with and without drag. The drag-free cases are not meant to be a realistic depiction but allow us to better isolate the effects of the individual magnetic forces.

We then are left with the choice of input parameters, both the seven that define the CME (v_F, M_{CME}, AW, $AW_\perp$, δ_{CS}, δ_{Ax}, and the magnetic field scaling $\beta = B_0/B_{SW}$) and how we decompose the front velocity into the bulk and expansion velocities. We consider three different scale CMEs a slightly faster than average CME (which we refer to as average for simplicity hereafter), a fast CME, and an extreme CME. As in Kay, Mays, and Verbeke (2020), which explored the sensitivity of the original ANTEATR to various input parameters, we expect to see different behavior for a CME that propagates at roughly the background solar wind speed as opposed to significantly faster than it. The initial properties for each CME are listed in Table 3. The mass, velocity, size, and magnetic field scaling all increase with CME scale.

For all cases, we assume that the CME begins at 10 R_s and stops at L1 (213 R_s). We use a C of 1.927 and a τ of 1 in the magnetic field model, which most closely mimics the Lundquist flux rope model that has been traditionally used to reconstruct in situ CMEs (Lepping et al., 1990). We assume solar wind values of a density of 6.9 cm^{-3}, velocity of 440 km/s, and magnetic field strength of 5.7 nT, which are based on OMNI database averages and the same as used in Kay, Mays, and Verbeke (2020). An exploration of the sensitivity to the CME, magnetic field model, and solar wind inputs will be presented in Paper II.

We use both the convective and self similar initial velocities decomposition (hereafter IVD) to split the front velocity into propagation and expansion velocities. This means that for each scale CME we run 16 simulations - 2 different IVD models, 4 different magnetic force configurations, and with and without background drag.

Table 1. Input Parameters for Different Scale CMEs

	Average	Fast	Extreme
v_F (km/s)	600	1250	2000
M_{CME} (10^{15} g)	2	10	50
AW (°)	30	45	60
$AW_\perp$ (°)	5	10	15
δ_{CS}	1	1	1
δ_{Ax}	0.7	0.7	0.7
β	1.33	3	8

4 Ensemble Study Results

4.1 CME Shape

Figure 2 shows the evolution of δ_{CS} with distance for all the ANTEATR-PARADE results. From left to right the columns show the average, fast, and extreme results. The top row shows results without drag and the bottom row includes the effects of drag. Within each panel, the dashed lines show results with a convective IVD and the solid lines represent the self-similar model. The line color indicates the force configuration with dark blue showing no forces, maroon showing only the CS pressure gradient, purple showing full CS forces, and light blue showing full CS and axial forces.

The most obvious trend is that the convective IVD leads to a much larger change in δ_{CS} for all scale CMEs, with or without drag. As the CME scale increases the difference between the convective and self-similar IVD decreases because the CME spends less time in transit and therefore less time pancaking.

For the self-similar IVD with no drag, there is no change in δ_{CS} from the initial value of one. Our choice of magnetic field model produces no asymmetry in the CS forces and therefore no variation in δ_{CS}. This will not hold true for variations in the magnetic field model, which we will explore in a future work.

For a convective IVD, the symmetric CS magnetic forces act to slow down the rapid pancaking driven by the initial velocities. With no magnetic forces, δ_{CS} quickly decreases in the first 50 R_s of propagation then gradually continues to decline until 1 AU. Including magnetic forces causes this rapid decrease to cease after about 10 R_s as the uniform outward acceleration counteracts the initially asymmetric CS expansion velocities. Not including the CS tension (maroon line) results in the strongest outward acceleration and the least change in δ_{CS}. The difference between any cases with magnetic forces is negligible compared to the difference with no magnetic forces. For the fast and extreme CMEs, we find that δ_{CS} begins slowly begins increasing around 50 R_s.

When we include drag it not only creates additional forces acting upon the CME but increases the transit time allowing for greater effects from any asymmetric accelerations or velocities. For the fast and extreme convective IVD cases, the drag causes δ_{CS} to continue to slightly decrease beyond 50 R_s rather than showing the slight increase of the drag-free cases.

We see a slight decrease in δ_{CS} for all the self-similar IVD cases with little difference between different magnetic force configurations. The pancaking is most noticeable for the fast case. The average case experiences weaker drag forces because its velocity differs the least from the background solar wind. The extreme case has the largest velocity difference but also the highest mass and spends the least time in transit.

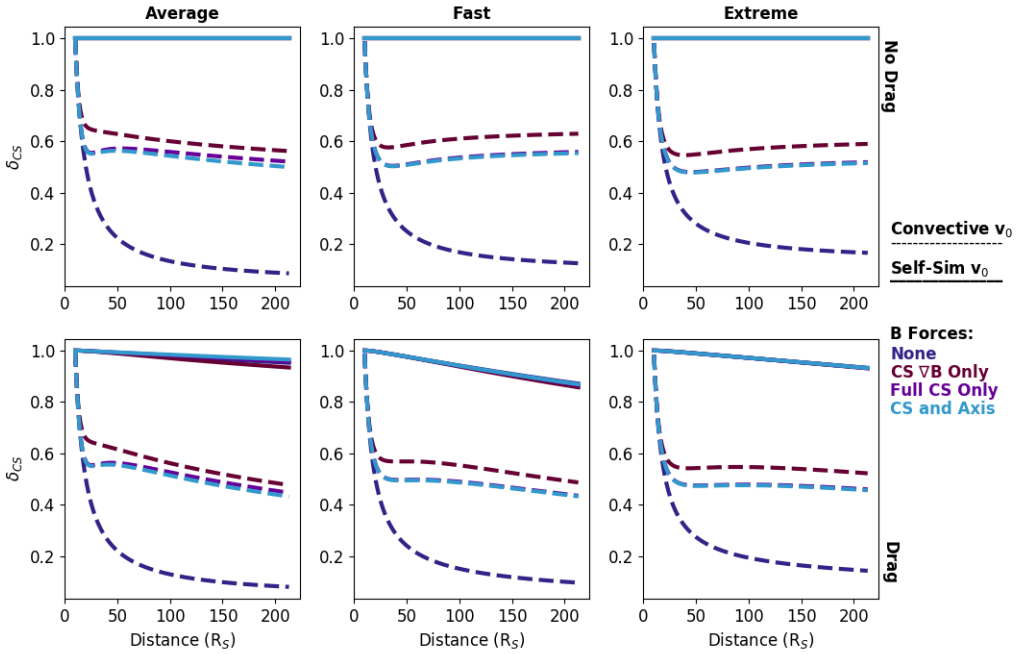

Figure 2. Change in the shape of the cross section during propagation from 10 R_S to 1 AU. The top row shows results without any drag and the bottom row includes drag. From left to right, each column shows results for the average, fast, and extreme CME. The dashed lines show results with a convective initial velocity and the solid lines have a self-similar initial velocity. Different line colors indicate different forces used in the model, as indicated by the legend.

We find that the choice of IVD has the largest effect on the amount of pancaking that a CME experiences. Within our cases we see that a convective IVD can cause δ_{CS} to change by 0.9 for an average CME with no other forces. In comparison, the drag forces only cause a maximum change of 0.13, seen for the fast CME. It remains to be seen the extent to which CS magnetic forces could change δ_{CS} if a magnetic field model was used that did not generate a symmetric acceleration.

Figure 3 has the same format as Fig. 2 but shows results for δ_{Ax}. Again, the results are largely dominated by the choice of IVD with a convective IVD causing a large change in δ_{Ax} and a self-similar IVD causing none on its own. The CS forces do not affect δ_{Ax} and the axial forces only produce a negligible change with convective IVD. The axial forces only produce a maximum change of 0.03 for the average CME with self-similar IVD. The inclusion of drag causes an additional change in δ_{Ax} of 0.03 to 0.07 for both the convective and self-similar IVD cases.

For both δ, we find that that the internal magnetic forces cause little distortion in the CME shape. Drag has a larger effect but the distortion is essentially determined by the initial expansion values we give the CME. This suggests that if we wish to accurately predict the shape of a CME at 1 AU we must fully understand its expansion within the low to mid corona as interplanetary effects appear to be less important. We, however, have only looked at one set of parameters (m, n, C, τ) for our very flexible magnetic field model and a single magnetic field strength scaling β for each CME. Particularly for the average CME, we pick a relative;y low value of β because a strong axial tension force can cause δ_{Ax} to become negative, meaning that the CME axial curvature is inverted, which ANTEATR-PARADE is currently not capable of handling. Variations with C, τ, and

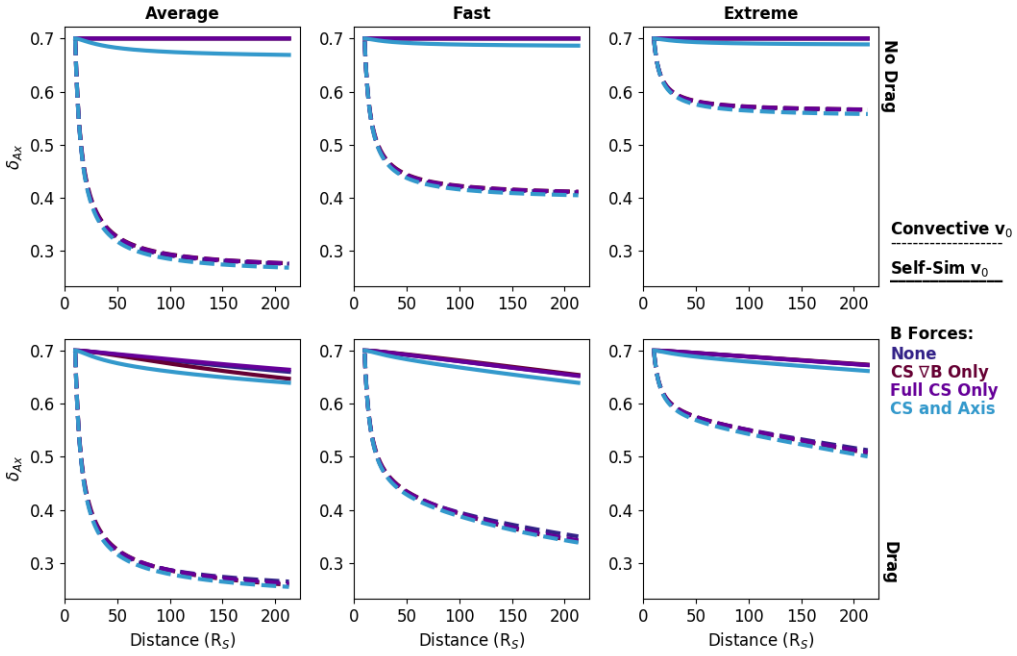

Figure 3. Same as Fig. 2 but for the axis shape.

β are explored in Paper II and future work will extend ANTEATR-PARADE to different values of m and n.

4.2 CME Size

Figure 4 shows the change in AW with radial distance in the same format as Fig. 2. To facilitate comparison, all panels have the same extent of 15° in the vertical axis but shifted to the range appropriate for that scale CME.

When there are no forces there is no change in the angular width, as expected. Comparing different force models, IVD, and drag configurations, we find that within each scale these variations lead to only about a 5° spread in the final angular width.

The angular width is affected by both the size of the toroidal axis and the CS. Not including CS tension leads to the largest AW due to the large CS expansion. We find little difference whether the axial forces are includes or not, though inclusion tends to lead to slightly smaller AW suggesting that the axial forces tend to be directed more inward than outward (axial tension exceeds the hoop force).

Adding drag allows for more time for the CME to expand during propagation leading to slightly larger CMEs than the drag-free counterparts. For all cases with magnetic forces, the AW never fully flattens out, there is a continued slight increase all the way to 1 AU.

We see the most rapid expansion in the first 10-20 R_s of propagation. Our choice of input parameters often create CMEs are that initially out of equilibrium, having at least a slight overpressure relative to the background solar wind. If our parameters start closer to equilibrium then we would only expect the gradual increase we see over long distances.

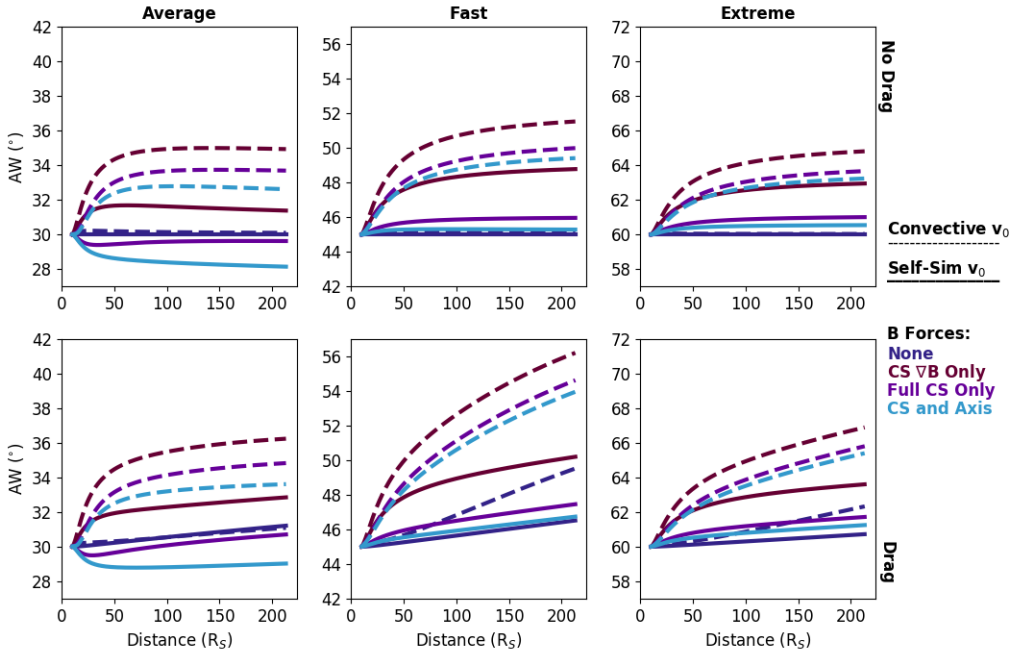

Figure 4. Same as Fig. 2 but for the angular width.

The convective IVD cases tend to have slightly larger AW than the corresponding self-similar IVD. The convective cases quickly become thinner in the radial direction, leading to higher magnetic energy density as the different IVD cases are initiated at the same size and with the same magnetic field strength. This creates stronger magnetic forces, ultimately leading to more expansion in the CS, as we see in Figure 5, which is analogous to Fig. 4 but for the perpendicular angular width. Note that the panels the same extent of 15° in the vertical direction, suggestion we see a comparable amount of CS expansion as for the full AW for all scale CMEs. This is only a few degrees, however, for most cases and mostly occurs during the rapid expansion phase close to the Sun.

As for AW, we find not including both magnetic or drag forces leads to no expansion, not including CS tension leads to the largest expansion, and including drag increases the expansion. The convective IVD leads to more expansion than the self-similar IVD, though the behavior is not terribly dissimilar for the fast and particularly the extreme cases without drag. With drag, the magnitude of the gradual expansion (beyond 30 R_s) actually exceeds that of the early rapid expansion (below 30 R_s) but for any of the cases including CS tension it is less than a few degrees of total expansion. For the average CME with drag and CS tension we actually see an initial decrease in $AW_\perp$ but it is less than a degree and it slowly begins increasing in the gradual phase.

For both angular widths we typically see an initial rapid increase below about 30 R_s, followed by a gradual increase all the way out to 1 AU. The total change in either angular width is never more than a few degrees whenever both components of the CS force are included. Further work needs to be done to explore different magnetic field models and strengths but this preliminary work suggests that the assumption of constant angular width during interplanetary propagation is a reasonable simplification for many situations.

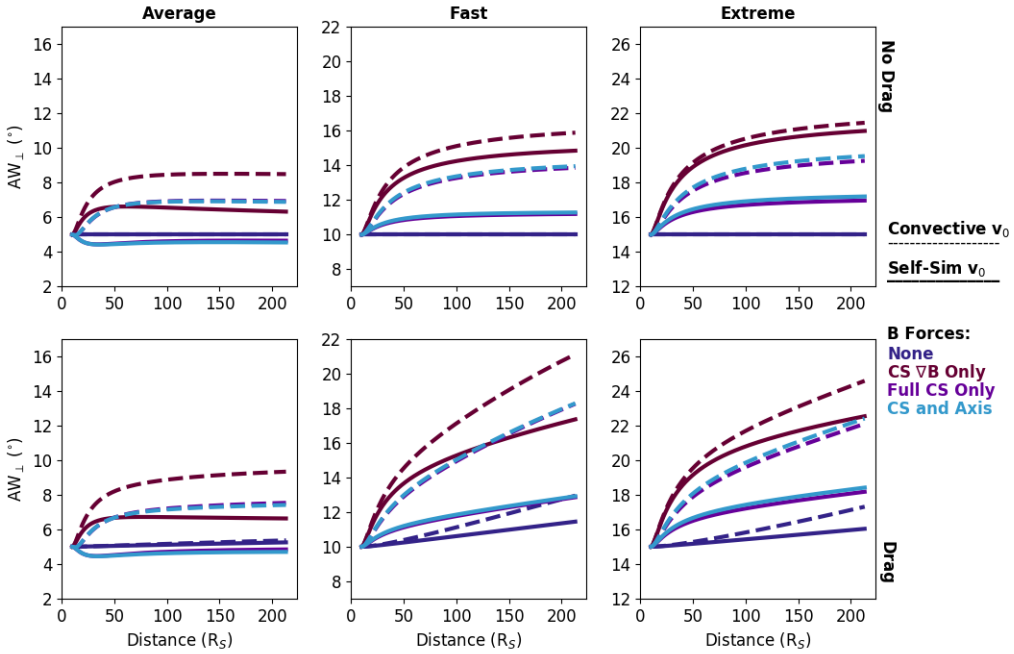

Figure 5. Same as Fig. 2 but for the perpendicular angular width.

4.3 CME Velocity

We now consider the evolution of the CME velocity. Figure 6 is similar to the previous figures. Each panel has the same format and the top and bottom rows still show results without and with drag. Now, from left to right the columns show the velocity of the CME front, the expansion velocity of the CS in the radial direction, and the expansion velocity of the CS in the perpendicular direction. We only show results for the fast CME. The general behavior tends to be the same for all scales and we will comment on any difference in the magnitude of the effects where appropriate.

Without drag the only changes in the velocity come from the magnetic forces. Similar to the expansion, for the drag-free cases we see an initial phase with rapid change followed by extended gradual change. The gradual phase seems to start around 20 R_s for the velocity as compared to the 30 R_s for the expansion. The CS tension-free cases have the largest increase in v_F due to the rapid CS expansion. Adding the CS tension constrains this and greatly decreases the acceleration of v_F. Adding the axial forces causes a further decrease. For the self-similar IVD, the full magnetic forces leads to nearly constant v_F, whereas we see an increase of about 100 km/s with the convective IVD.

The cases that had an increase in v_F when drag was not included show a similar increase when drag is included but the v_F quickly begins to decrease as the CME is decelerated by the background solar wind. For each IVD option, the different magnetic force combinations cause different behavior close to the Sun but by the time the CME reaches 1 AU the models have all converged to a single v_F. This highlights the greater importance of the drag force relative to the magnetic forces. We note that for the extreme scale CME the convergence to a single v_F is less pronounced. The final v_F is consistently higher for the self-similar IVD cases than the convective IVD cases. The convective IVD cases tend to be larger in both AW and $AW_\perp$ and therefore experience more drag, which leads to more deceleration.

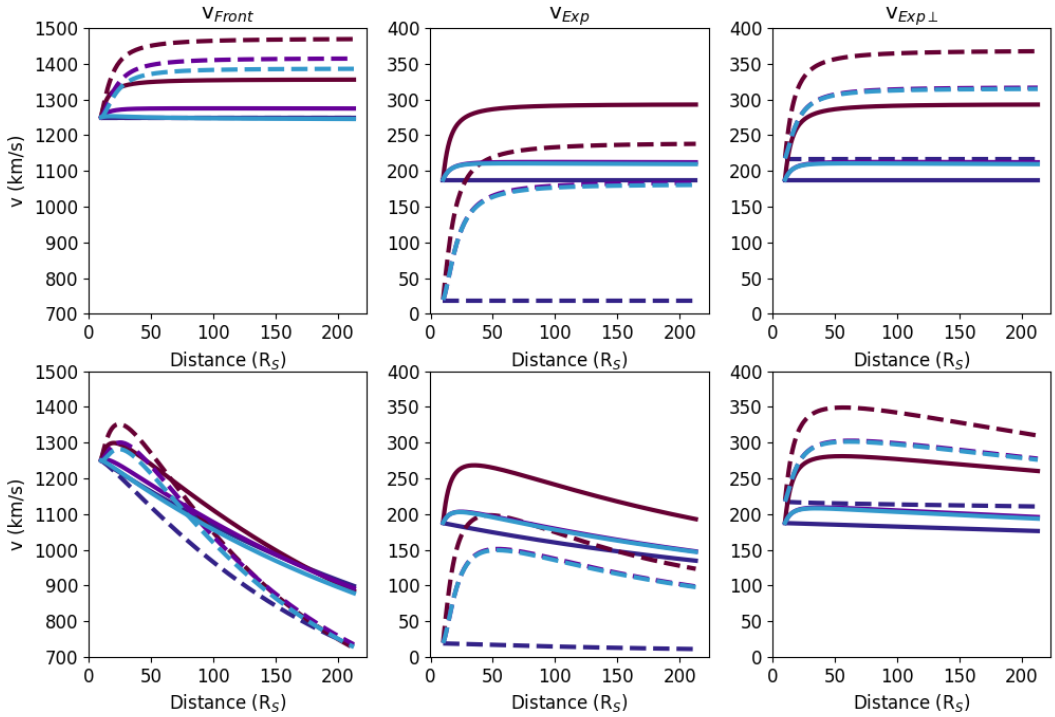

Figure 6. Change in velocity for several different velocities. The panels are analogous to Fig. 2 but the columns show the front velocity, radial expansion velocity, and perpendicular expansion velocity, from left to right.

The middle column shows the expansion speed of the CS in the radial direction. This is most likely the expansion speed one would infer from an in situ profile assuming an impact near the center of the CS, but the observed value will change by a geometrical factor as the impact moves toward the edge. The figure shows that a convective IVD gives an initial v_{Exp} that is about a factor of four smaller than the v_{Exp} from the self-similar IVD. With no magnetic or drag forces, v_{Exp} remains constant. The magnetic forces cause v_{Exp} to increase with the cases only including CS pressure gradients accelerating the most and the inclusion of axial forces differing little from the full CS forces case. For full magnetic forces with no drag, the final v_{Exp} for the convective and self-similar IVD only differ by about 25 km/s but reach these values by different means. The self-similar case rapidly accelerates out to about 30 R_s then very slowly decelerates for the rest of the duration. The convective case rapidly accelerates close to the Sun, then the acceleration slows down around 20 R_s but slowly continues until the CME reaches 100 R_s, after which v_{Exp} begins negligibly decreasing. The final value of v_{Exp} seems to be more strongly influenced by the background and magnetic forces than the initial decomposition of the velocity, unlike most of the other outputs we have considered thus far. We note that the final v_{Exp} are more dissimilar for the extreme case so the similarity may just be a coincidence for this case.

When we include drag v_{Exp} initially increases, as before, but the drag forces cause the profile to turn over and begin decelerating. For the convective case the deceleration begins around 50 R_s whereas it starts much closer, around 25 R_s, for the self-similar case. This hints at the magnetic forces being dominant early on for the convective case. Here the final v_{Exp} differ by 50 km/s, a bit more than seen in the drag free cases.

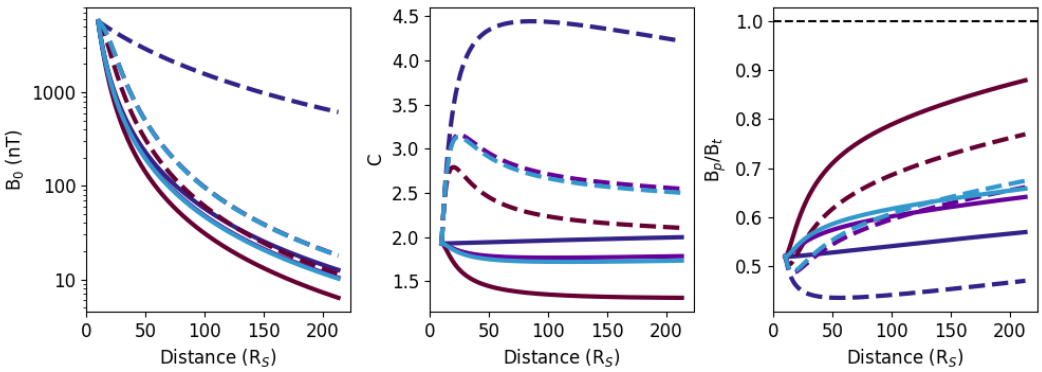

Figure 7. Change in magnetic field parameters. All panels show results including drag. The panels show B_0, C, and the ratio of B_p to B_t.

The right column shows the change in the expansion speed of the CS in the perpendicular direction, $v_{Exp\perp}$. Here the convective case has an initial $v_{Exp\perp}$ that is similar to but slightly higher than the self-similar case. Without drag, the behavior of $v_{Exp\perp}$ for the self-similar case is identical to that of v_{Exp} since these velocities are initially similar and the magnetic forces create a uniform acceleration of the CS. The values differ for the convective cases because their initial values are dissimilar. The timing of the rapid acceleration in $v_{Exp\perp}$ for the convective cases is now more similar to the self-similar cases as opposed to the prolonged increase that we saw in v_{Exp}.

Including drag again causes a turn over in the velocity profile, though here the deceleration is less drastic as the velocity differential between the perpendicular expansion velocity and the background solar wind is much smaller than in the perpendicular direction. We see a difference of 75 km/s in final velocities of the different IVD models with full magnetic forces, suggesting that $v_{Exp\perp}$ could be a useful metric for inferring the initial expansion velocities of CMEs, assuming we could find a manner to accurately measure it.

4.4 CME Magnetic Field

Figure 7 show the change in the magnetic field model parameters for the fast CME including the effects of drag. We do not find a significant difference in the magnetic parameters with and without drag. The left panel shows B_0, which sets the magnitude of magnetic field and has a log scale on the vertical axis unlike all the other panels and figures. The magnetic field rapidly decreases as the CME expands. The convective IVD decomposition leads to stronger B_0 since the CME CS becomes very compressed in the radial direction. When the convective approach is combined with no magnetic forces it leads to a magnetic field strength of 220 nT that is clearly inappropriately strong at 1 AU. Beyond this outlier, the variation in B_0 is less pronounced than some of the other outputs we have considered. Most have a final B_0 between 10 and 13 nT but the full CS forces, with or with axial forces, are only slightly higher at about 18 nT, and the self-similar IVD with only CS pressure gradients slightly lower at about 6 nT.

The middle panel shows the change in C, which represents the scaling between the poloidal and toroidal field. We assume a constant τ of 1 and we expect the flux rope to become kink unstable for a C below 1.7 according to Florido-Llinas et al. (2020). C rapidly increases for the convective IVD due to the pancaking more strongly contracting the area for the toroidal flux relative to the change in the area for the poloidal flux. With any

magnetic forces, C begins decreasing around 30 R_s as the disparity in the expansion velocities is washed out from the magnetic accelerations.

Conversely, the cases with self-similar IVD have C initially decrease then approach a constant value. The CS tension-free case continues decreasing out to farther distances, reaching a final value of 1.31, clearly below the limit for the kink instability. The force free case does not change because the CME retains the same shape. Both cases with full CS forces approach the kink limit but do not cross it with the case including axial forces staying slightly larger (1.78 versus 1.73).

The right column shows the ratio of the toroidal magnetic field at the center of the CME and the poloidal magnetic field at the nose of the CME. The ratio of the two is

$$\frac{B_p}{B_t} = \frac{2}{C(1+\delta_{CS}^2)} \tag{22}$$

where we have assumed a τ of one. In general, the poloidal field tends to increase relative to the toroidal field during propagation but never becomes greater than it, except for the force-free, convective IVD case that we already determined was unrealistic from its B_0. The behavior for the convective IVD case is similar to that of their C values, an initial increase followed by a slow decrease if any magnetic forces are included. Note, though, that the ratio is inversely proportional to C so the change in δ_{CS} must have a larger effect than the change in C. The change in the ratio is much more gradual for the self-similar IVD cases with a slow increase occurring all the way to 1 AU. Once again, we find including the axial forces makes little difference.

5 Relevance to Space Weather Forecasting

While the evolution of parameters with distance is interesting and allows us a deeper understanding of the physics involved, the primary benefit of an efficient, simplified model like ANTEATR-PARADE is to eventually provide values relevant to space weather forecasting. Some of these are direct outputs from the model that we have already considered while others are calculated from the outputs. Figure 8 shows the front and expansion velocity (top left), toroidal and poloidal field strength (top right), duration and transit time (bottom left), and number density and estimated maximum Kp (bottom right). All values that vary with distance are taken at the time the CME nose reaches 1 AU. The parameters are grouped based on similarity for display, we are not actively looking for unexpected correlations, rather just the spread in each parameter, but we do see the expected correlations for the velocity and magnetic field strength pairs. Each panel contains the results for all 24 model configurations that include drag. The color represents the CME scale with blue being average, maroon being fast, and purple being extreme. The symbol shape represents the magnetic force configuration with a triangle representing none, a star representing only CS pressure gradients, a square representing the full CS forces, and a circle representing full CS and axial forces. Filled symbols correspond to simulations with a self-similar IVD decomposition and empty symbols are convective.

The top left panel shows the front velocity and the expansion velocity of the CS in the radial direction. The different scale CMEs separate in the horizontal direction due to the large variance in their v_F. For the average and fast CMEs there is almost no spread in v_F due to different magnetic force model configurations but they do cause a bit of a spread for the extreme cases with no magnetic forces being the slowest and only CS pressure gradients being the fastest. The IVD can influence the final v_F by hundreds of km/s.

The spread in the radial CS expansion velocity is comparable the spread in the front velocities when any magnetic forces are included (note the difference in range of the axes). The spread in the front velocity can be broken down into the spread in the bulk, axis, and radial CS expansion velocity. The similarity in the spread of the two velocities suggests the CS expansion is the largest factor in determining the precise value of the front

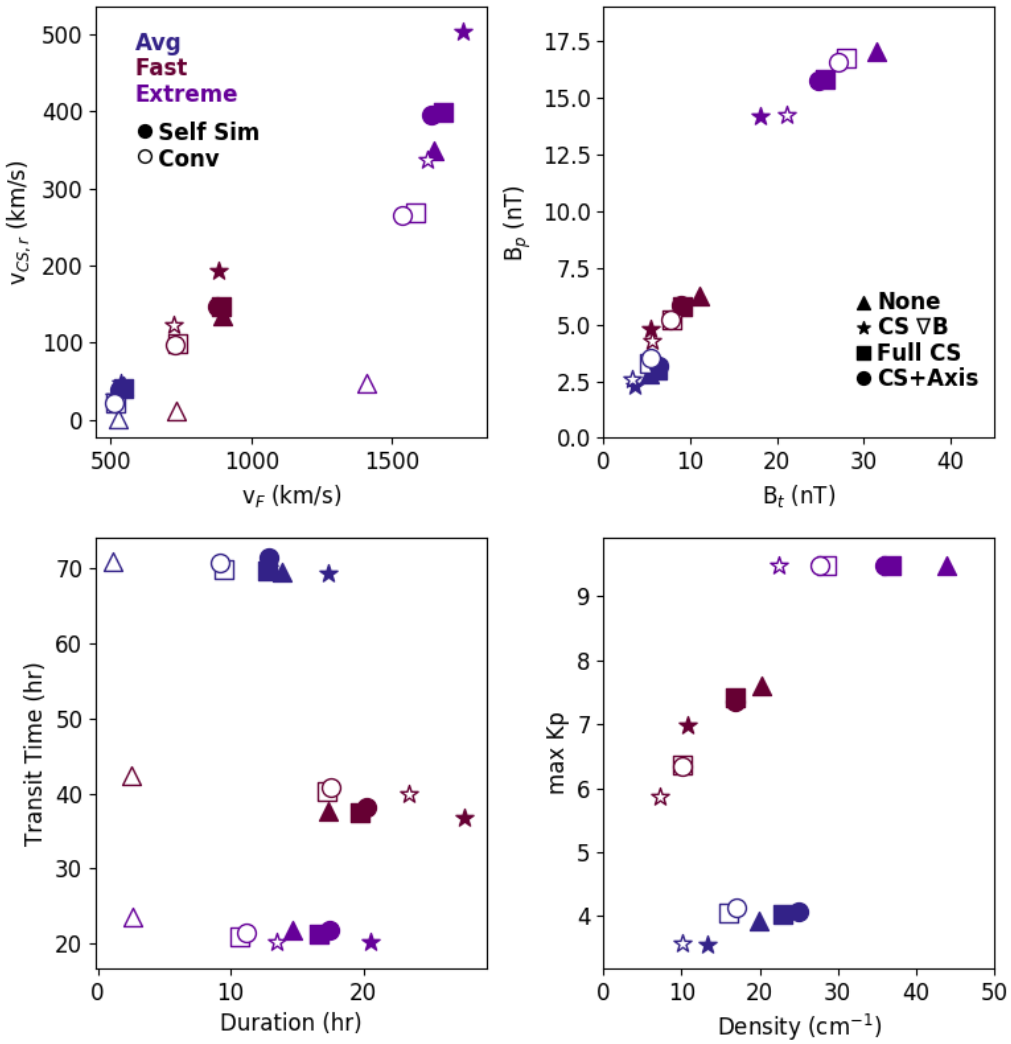

Figure 8. Comparison of the 1 AU values of the front and radial expansion velocities (top left), B_t and B_p (top right), the duration and transit time (bottom left), and the number density and maximum Kp at the CME front (bottom left).

velocity at 1 AU. The drag force certainly contributes more to the total decrease in v_F for a fast or extreme CME, but the effects do not differ significantly between different model configurations, so we must not be seeing strong second-order effects from the magnetic forces changing the AW then affecting the total drag and therefore v_F.

The top right panel shows the toroidal and poloidal magnetic field strength at 1 AU. Both components increase with CME scale as a result of our choice of the initial magnetic field strength. The components are highly correlated as they both depend linearly on B_0. B_t tends to be stronger than B_p because of our choice of C. Interestingly, for the average and fast CME we find very little spread in both components when any magnetic forces are included, only a few nT in B_p and about 5 nT in B_t. The extreme case shows more variation, almost 5 nT in B_p and 15 nT in B_t. The cases with only CS pressure gradients have the smallest magnetic field due to their excessive expansion and the cases with no forces have the strongest field due to the pancaking. In general, there is not a consistent trend with respect to the initial IVD choice. The combination of no forces and convective IVD leads to excessively high magnetic field components, with the average and fast having a total magnetic field strength of around 40 nT and the extreme case around 130 nT (and outside the range of the figure).

The bottom left panel shows the transit time and estimated CME duration, calculated from the CS width and velocities (including expansion) upon impact. We see little variation in the transit time within each CME scale, no more than a few hours. From this and our previous studies (Kay, Mays, & Verbeke, 2020), we know the transit time is very sensitive to the CME parameters but it does not seem the choice of magnetic forces nor does the initial velocity decomposition make a significant difference.

The duration, however, is quite sensitive to the model variations. Convective IVD with no force is an outlier with very short duration due to the pancaking. Ignoring this outlier, the remaining cases still have a spread of approximately 10 hours in the duration. The convective cases all have shorter duration than their self-similar counterparts and the cases without CS tension have the longest duration since they experience the most expansion. These results suggest that comparison with an observed duration could be a useful metric for distinguishing the correct breakdown of the initial velocity.

Finally, the bottom right panel shows the number density and an estimated maximum Kp. We calculate the Kp the same as Kay, Nieves-Chinchilla, and Jian (2020), which was based on the empirical expression in Mays et al. (2015)

$$Kp = 9.5 - \exp\left[2.17676 - 0.000052 v^{4/3} B_{\perp}^{2/3} \sin^{8/3}\frac{\theta_C}{2}\right] \tag{23}$$

Here, $B_\perp$ is the transverse component of the magnetic field in Geocentric Solar Magnetospheric coordinates and θ_C is the clock angle of the magnetic field. We use B_p for $B_\perp$ so that we are calculating Kp when the front of the CME first impacts and assume a fully southward clock angle so that this is the maximum expected Kp.

For the Kp, we see little variation within the average and extreme scale CMEs but for different reasons. The average CME is weak so the Kp is small to begin with but the extreme CME is so powerful that all Kp values are essentially the maximum possible value of 9.5 from the empirical expression. We see more variation for the fast CME with Kp varying by about 2, the self-similar cases having higher values than the convective cases, and no CS tension causing the lowest Kp.

For all cases we see a large spread of 15-25 cm^{-1} in the number density, which results from the variety we see in the amount of expansion between the different cases. The convective cases and cases without CS tension tend to have the lowest density. It appears that comparison with the observed number density could also be useful for distinguishing between different models.

6 Discussion

With this work, we have demonstrated the capabilities of ANTEATR-PARADE and shown that it produces reasonable results, but we have not yet validated it at all against observations. Ideally, we would compare the entire profile with values reconstructed from observations from coronagraphs and heliospheric imagers. These observations are readily available and the reconstruction techniques are well-established. We strongly suspect, however, that the uncertainties from the reconstruction techniques are sufficiently large that they would not be of significant use for validation beyond seeming correct in general. Of more use, most likely, will be comparison with the final in situ parameters as we can measure those more directly and more accurately. We have an abundance of 1 AU measurements but comparisons at other distances with Parker Solar Probe or Solar Orbiter observations would be critical for validating the full model and helping constrain the early CME evolution.

We notice that many of the CME properties have two distinct phases with rapid change early on followed by gradual change at farther distances. This is quite similar to the second two phases of the three phase model for a CME's radial propagation in the corona (Zhang & Dere, 2006). All the forces we consider should be acting upon the CME in the corona, our choice of starting simulations at 10 R_s is somewhat arbitrary. It is simply where we previously started the original ANTEATR simulations, which were designed to follow ForeCAT simulations that ran to 10 R_s because beyond this the external magnetic deflection and rotation forces become negligible. We hypothesize that we may be initiating ANTEATR-PARADE CMEs unnecessarily out of equilibrium and that if we begin simulating the internal magnetic forces closer to the Sun the rapid change phase may be more concurrent with the rapid radial acceleration phase. We believe that the general results in the paper are still worthwhile, even if the CMEs are initially unbalanced, because they seem to rapidly re-equilibrate within the first 10-20 R_s. Right now, we cannot simply start the ANTEATR-PARADE simulations much closer to the Sun as it currently uses a very simplified model of the background solar wind.

We have also only considered a single set of parameters [m, n] defining our magnetic field model. The chosen pair happen to correspond to magnetic forces that uniformly affect the expansion of the cross section and therefore cannot induce any new asymmetry. Exploration of other pairs of [m, n] will be critical for determining the extent to which magnetic forces can alter CME cross-sectional shape.

Future work will incorporate these internal magnetic forces into ForeCAT and we can then use those results to potentially initiate ANTEATR-PARADE simulations more appropriately. Another step is to propagate these advancements in our CME structure and magnetic field into the FIDO model. Adding the elliptical cross section and more flexible magnetic field model into FIDO, the in situ magnetic field model, should help us more accurately reproduce, and eventually predict, the space weather effects of CMEs.

7 Conclusion

We present the first results from ANTEATR-PARADE, which uses internal magnetic and external drag forces to simulate the propagation, expansion, and deformation of a CME in interplanetary space. We analyze the relative contribution of the different forces and find that the drag forces tend to have a larger effect than the magnetic forces, at least for the single parameterization of the magnetic field model used in this work.

We consider two methods for breaking down the total initial speed of a CME front into bulk and expansion components and find that the expansion and deformation are quite sensitive to the chosen values but the propagation less so. We propose that ANTEATR-PARADE could be particularly useful for helping diagnose the early behavior of CMEs than may be difficult to disentangle in coronal observations. Since it is so sensitive to

certain initial properties or model configurations we can potentially constrain them by comparing the outputs to observed events.

Since the effects of the initial velocities tend to outweigh the internal magnetic forces we find that velocities that lead to pancaking produce CMEs with thinner radial widths, as expected, but also larger face-on and edge-on angular widths. The larger size leads to slower speeds of the CME front due to the increased drag. Despite the lower velocities, we find shorter durations as the effects are dominated by the decreased radial width due to pancaking. For most cases, the magnetic field strength at 1 AU is not particularly sensitive to the model configuration, suggesting that some of the effects (such as larger widths in the perpendicular direction but shorter in the radial direction) largely cancel out.

We note that the model is still sensitive to the magnetic forces, just less so than sensitivity to the initial velocities. In particular, if any magnetic forces are included then the magnetic tension from the poloidal magnetic field needs to be include otherwise the cross sections quickly become unnaturally large. The axial forces tend to be weaker than the ones acting on the cross section but can still be important in determining whether the flux rope evolves in a manner that would be kink unstable.

Acknowledgments

C. Kay would like to thank S. K. W. L. Kay III for his support during this work.

References

Florido-Llinas, M., Nieves-Chinchilla, T., & Linton, M. G. (2020, July). Analysis of the Helical Kink Stability of Differently Twisted Magnetic Flux Ropes. *arXiv e-prints*, arXiv:2007.06345.

Heinemann, S. G., Temmer, M., Farrugia, C. J., Dissauer, K., Kay, C., Wiegelmann, T., ... Carcaboso, F. (2019, September). CME-HSS Interaction and Characteristics Tracked from Sun to Earth. , *294*(9), 121. doi: 10.1007/s11207-019-1515-6

Hess, P., & Zhang, J. (2015, October). Predicting CME Ejecta and Sheath Front Arrival at L1 with a Data-constrained Physical Model. *The Astrophysical Journal*, *812*, 144. doi: 10.1088/0004-637X/812/2/144

Hidalgo, M. A., Cid, C., Vinas, A. F., & Sequeiros, J. (2002, January). A non-force-free approach to the topology of magnetic clouds in the solar wind. *Journal of Geophysical Research (Space Physics)*, *107*(A1), 1002. doi: 10.1029/2001JA900100

Isavnin, A. (2016, December). FRiED: A Novel Three-dimensional Model of Coronal Mass Ejections. *The Astrophysical Journal*, *833*, 267. doi: 10.3847/1538-4357/833/2/267

Janvier, M., Démoulin, P., & Dasso, S. (2013, August). Global axis shape of magnetic clouds deduced from the distribution of their local axis orientation. *Astronomy and Astrophysics*, *556*, A50. doi: 10.1051/0004-6361/201321442

Kay, C., & Gopalswamy, N. (2018, Sep). The Effects of Uncertainty in Initial CME Input Parameters on Deflection, Rotation, B_z, and Arrival Time Predictions. *Journal of Geophysical Research (Space Physics)*, *123*(9), 7220-7240. doi: 10.1029/2018JA025780

Kay, C., Gopalswamy, N., Reinard, A., & Opher, M. (2017, February). Predicting the Magnetic Field of Earth-impacting CMEs. *The Astrophysical Journal*, *835*, 117. doi: 10.3847/1538-4357/835/2/117

Kay, C., Mays, M. L., & Verbeke, C. (2020, January). Identifying Critical Input Parameters for Improving Drag-Based CME Arrival Time Predictions. *Space Weather*, *18*(1), e02382. doi: 10.1029/2019SW002382

Kay, C., & Nieves-Chinchilla, T. (2021). Modeling Interplanetary Expansion and Deformation of CMEs with ANTEATR-PARADE II: Sensitivity to Input Parameters. *Journal of Geophysical Research (Space Physics)*.

Kay, C., Nieves-Chinchilla, T., & Jian, L. K. (2020, February). FIDO-SIT: The First Forward Model for the In Situ Magnetic Field of CME-Driven Sheaths. *Journal of Geophysical Research (Space Physics)*, *125*(2), e27423. doi: 10.1029/2019JA027423

Kay, C., Opher, M., & Evans, R. M. (2015, June). Global Trends of CME Deflections Based on CME and Solar Parameters. *The Astrophysical Journal*, *805*, 168. doi: 10.1088/0004-637X/805/2/168

Kilpua, E. K. J., Lugaz, N., Mays, M. L., & Temmer, M. (2019, April). Forecasting the Structure and Orientation of Earthbound Coronal Mass Ejections. *Space Weather*, *17*(4), 498-526. doi: 10.1029/2018SW001944

Lepping, R. P., Burlaga, L. F., & Jones, J. A. (1990, August). Magnetic field structure of interplanetary magnetic clouds at 1 AU. *Journal of Geophysical Research*, *95*, 11957-11965. doi: 10.1029/JA095iA08p11957

Liu, J., Ye, Y., Shen, C., Wang, Y., & Erdélyi, R. (2018, March). A New Tool for CME Arrival Time Prediction using Machine Learning Algorithms: CAT-PUMA. *The Astrophysical Journal*, *855*, 109. doi: 10.3847/1538-4357/aaae69

Mays, M. L., Taktakishvili, A., Pulkkinen, A., MacNeice, P. J., Rastätter, L., Odstrcil, D., ... Kuznetsova, M. M. (2015, June). Ensemble Modeling of CMEs Using the WSA-ENLIL+Cone Model. *Solar Physics*, *290*, 1775-1814. doi: 10.1007/s11207-015-0692-1

Mishra, W., & Wang, Y. (2018, September). Modeling the Thermodynamic Evolution of Coronal Mass Ejections Using Their Kinematics. , *865*(1), 50. doi: 10.3847/1538-4357/aadb9b

Möstl, C., Rollett, T., Frahm, R. A., Liu, Y. D., Long, D. M., Colaninno, R. C., ... Vršnak, B. (2015, May). Strong coronal channelling and interplanetary evolution of a solar storm up to Earth and Mars. *Nature Communications*, *6*, 7135. doi: 10.1038/ncomms8135

Mulligan, T., & Russell, C. T. (2001, June). Multispacecraft modeling of the flux rope structure of interplanetary coronal mass ejections: Cylindrically symmetric versus nonsymmetric topologies. , *106*(A6), 10581-10596. doi: 10.1029/2000JA900170

Napoletano, G., Forte, R., Moro, D. D., Pietropaolo, E., Giovannelli, L., & Berrilli, F. (2018, Feb). A probabilistic approach to the drag-based model. *Journal of Space Weather and Space Climate*, *8*, A11. doi: 10.1051/swsc/2018003

Nieves-Chinchilla, T., Linton, M. G., Hidalgo, M. A., & Vourlidas, A. (2018, July). Elliptic-cylindrical Analytical Flux Rope Model for Magnetic Clouds. , *861*(2), 139. doi: 10.3847/1538-4357/aac951

Owens, M., & Cargill, P. (2004, December). Non-radial solar wind flows induced by the motion of interplanetary coronal mass ejections. *Annales Geophysicae*, *22*(12), 4397-4406. doi: 10.5194/angeo-22-4397-2004

Owens, M. J., Cargill, P. J., Pagel, C., Siscoe, G. L., & Crooker, N. U. (2005, Jan). Characteristic magnetic field and speed properties of interplanetary coronal mass ejections and their sheath regions. *Journal of Geophysical Research (Space Physics)*, *110*(A1), A01105. doi: 10.1029/2004JA010814

Owens, M. J., Lockwood, M., & Barnard, L. A. (2017, June). Coronal mass ejections are not coherent magnetohydrodynamic structures. *Scientific Reports*, *7*, 4152. doi: 10.1038/s41598-017-04546-3

Palmerio, E., Kilpua, E. K. J., Möstl, C., Bothmer, V., James, A. W., Green, L. M., ... Harrison, R. A. (2018, May). Coronal Magnetic Structure of Earthbound CMEs and In Situ Comparison. *Space Weather*, *16*(5), 442-460. doi: 10.1002/2017SW001767

Paouris, E., & Mavromichalaki, H. (2017, December). Effective Acceleration Model

for the Arrival Time of Interplanetary Shocks driven by Coronal Mass Ejections. *Solar Physics*, *292*, 180. doi: 10.1007/s11207-017-1212-2

Patsourakos, S., Georgoulis, M. K., Vourlidas, A., Nindos, A., Sarris, T., Anagnostopoulos, G., ... Vlahos, L. (2016, January). The Major Geoeffective Solar Eruptions of 2012 March 7: Comprehensive Sun-to-Earth Analysis. , *817*(1), 14. doi: 10.3847/0004-637X/817/1/14

Riley, P., & Crooker, N. U. (2004, January). Kinematic Treatment of Coronal Mass Ejection Evolution in the Solar Wind. *The Astrophysical Journal*, *600*, 1035-1042. doi: 10.1086/379974

Riley, P., Linker, J. A., Lionello, R., Mikić, Z., Odstrcil, D., Hidalgo, M. A., ... Rees, A. (2004, October). Fitting flux ropes to a global MHD solution: a comparison of techniques. *Journal of Atmospheric and Solar-Terrestrial Physics*, *66*(15-16), 1321-1331. doi: 10.1016/j.jastp.2004.03.019

Riley, P., Mays, M. L., Andries, J., Amerstorfer, T., Biesecker, D., Delouille, V., ... Zhao, X. (2018, Sep). Forecasting the Arrival Time of Coronal Mass Ejections: Analysis of the CCMC CME Scoreboard. *Space Weather*, *16*(9), 1245-1260. doi: 10.1029/2018SW001962

Rollett, T., Möstl, C., Isavnin, A., Davies, J. A., Kubicka, M., Amerstorfer, U. V., & Harrison, R. A. (2016, Jun). ElEvoHI: A Novel CME Prediction Tool for Heliospheric Imaging Combining an Elliptical Front with Drag-based Model Fitting. *The Astrophysical Journal*, *824*(2), 131. doi: 10.3847/0004-637X/824/2/131

Russell, C. T., & Mulligan, T. (2002, Apr). On the magnetosheath thicknesses of interplanetary coronal mass ejections. *Planetary and Space Sciences*, *50*(5-6), 527-534. doi: 10.1016/S0032-0633(02)00031-4

Savani, N. P., Owens, M. J., Rouillard, A. P., Forsyth, R. J., Kusano, K., Shiota, D., & Kataoka, R. (2011, April). Evolution of Coronal Mass Ejection Morphology with Increasing Heliocentric Distance. I. Geometrical Analysis. *The Astrophysical Journal*, *731*, 109. doi: 10.1088/0004-637X/731/2/109

Thernisien, A. F. R., Howard, R. A., & Vourlidas, A. (2006, November). Modeling of Flux Rope Coronal Mass Ejections. *The Astrophysical Journal*, *652*, 763-773. doi: 10.1086/508254

Tousey, R. (1973). The solar corona. In M. J. Rycroft & S. K. Runcorn (Eds.), *Space research conference* (p. 713-730).

Vršnak, B., Žic, T., Vrbanec, D., Temmer, M., Rollett, T., Möstl, C., ... Shanmugaraju, A. (2013, July). Propagation of Interplanetary Coronal Mass Ejections: The Drag-Based Model. *Solar Physics*, *285*, 295-315. doi: 10.1007/s11207-012-0035-4

Welsch, B. T. (2018, July). Flux Accretion and Coronal Mass Ejection Dynamics. , *293*(7), 113. doi: 10.1007/s11207-018-1329-y

Wold, A. M., Mays, M. L., Taktakishvili, A., Jian, L. K., Odstrcil, D., & MacNeice, P. (2018, March). Verification of real-time WSA-ENLIL+Cone simulations of CME arrival-time at the CCMC from 2010 to 2016. *Journal of Space Weather and Space Climate*, *8*(27), A17. doi: 10.1051/swsc/2018005

Zhang, J., & Dere, K. P. (2006, October). A Statistical Study of Main and Residual Accelerations of Coronal Mass Ejections. *The Astrophysical Journal*, *649*, 1100-1109. doi: 10.1086/506903